Hindawi
International Journal of Energy Research
Volume 2024, Article ID 9990559, 14 pages
https://doi.org/10.1155/2024/9990559

Research Article

Ceiling of Barium Substitution for B-Site Cation in Organometal Halide Perovskite Solar Cells

Kai-Chi Hsiao,[1] **Ching-Mei Ho**,[1] **Ting-Han Lin**,[1] **Shih-Hsuan Chen**,[1] **Yin-Hsuan Chang**,[1] **Ying-Han Liao**,[1] **Jia-Mao Chang**,[1] **Tz-Feng Lin**,[2] **Yu-Ching Huang**,[1,3,4] **Kun-Mu Lee**,[1,3,4,5] **and Ming-Chung Wu**[1,3,4,5]

[1]*Department of Chemical and Materials Engineering, Chang Gung University, Taoyuan 33302, Taiwan*
[2]*Department of Fiber and Composite Materials, Feng Chia University, Taichung 40724, Taiwan*
[3]*Department of Materials Engineering, Ming Chi University of Technology, New Taipei City 24301, Taiwan*
[4]*Center for Sustainability and Energy Technologies, Chang Gung University, Taoyuan 33302, Taiwan*
[5]*Division of Neonatology, Department of Pediatrics, Chang Gung Memorial Hospital, Linkou, Taoyuan 33305, Taiwan*

Correspondence should be addressed to Tz-Feng Lin; tflin@fcu.edu.tw, Yu-Ching Huang; huangyc@mail.mcut.edu.tw, Kun-Mu Lee; kmlee@cgu.edu.tw, and Ming-Chung Wu; mingchungwu@cgu.edu.tw

Received 18 July 2023; Revised 28 November 2023; Accepted 1 December 2023; Published 23 January 2024

Academic Editor: Muhammad Ahsan Saeed

Significant advancements have been made in the development of perovskite solar cells (PSCs) in recent years, resulting in increased efficiency rates. Nonetheless, the presence of lead within these cells has become a pressing concern. Our study investigates the correlation between tolerance of barium substitution and A-site cation composition through systematic analysis of morphology, crystal structure, optical property, and carrier dynamics. The results show that a high barium substitution ratio of 15 mol.% can be achieved by inducing 60 mol.% of a large A-site cation, formamidinium, into the methylammonium-based perovskite. The induction of large A-site cations in barium-substituted perovskite overcomes the imbalance between hole and electron diffusion lengths, resulting in an electron and a hole diffusion length of 395 nm and 440 nm, respectively. The champion device for 15 mol.% barium-substituted perovskite, $FA_{0.6}MA_{0.4}Pb_{0.85}Ba_{0.15}I_{3-y}Cl_y$, achieves a PCE of 11.13%, which is the highest record for 15 mol.% of lead reduction. This study provides insights into the limitations of lead substitution in perovskite solar cells and highlights the ceiling for barium substitution ratio in mixed cation perovskite.

1. Introduction

Organic-inorganic lead halide perovskite solar cells (PSCs) have attracted significant attention as a potential candidate for next-generation green energy due to their outstanding photovoltaic characteristics: long exciton diffusion length, high absorption coefficient, relatively low cost, and large processing window [1–3]. Notably, PSCs have achieved a significant milestone in photovoltaics, with reported power conversion efficiencies (PCE) surpassing 26% [4]. Three-dimensional (3D) perovskites with the general formula ABX_3 (A: organic ammonium cation; B: group IV A metal; and X: halogen) have emerged as popular absorber materials in perovskite solar cells (PSCs). Although lead-based perovskite devices have exhibited remarkable photovoltaic performance, the presence of lead in the active layer raises significant concerns [5–7]. Extensive efforts have been devoted to addressing the issue of lead and mitigating its adverse effects on the sustainability of PSCs [8–11]. Tin, which shares similar chemical properties, becomes the first intuitive replacement for lead in conventional PSCs [12–14]. However, the electron configuration of tin predisposes it to oxidation from a divalent cation to a more stable quadrivalent cation in ambient conditions, leading to the loss of its photovoltaic properties [15, 16]. Another alternative is to explore lead-free perovskite derivatives such as the double perovskite $Cs_2AgBiBr_6$ or rudorffite materials like Ag_3BiI_6 [17, 18]. Despite the high stability of these lead-

free perovskite-derivative materials, their photovoltaic performance remains inferior to that of conventional lead-based PSCs, making them lag behind the progress of lead-based PSCs [19, 20].

To prevent the toxic element of lead from being released, several lead-capturing strategies have been developed to mitigate lead leakage from lead-based PSCs. A donor-acceptor type polymer modified with alkoxy side chains has been reported to possess the ability to chelate the lead ion when it is applied as a hole transport layer in conventional PSC architecture (n-i-p). Approximately 80% of the lead leakage can be captured through the functionalized polymer. This strategy is believed to prevent possible lead leakage from lead-based PSCs when they are subjected to ambient air conditions [21]. An in situ polymerization strategy is also applied to alleviate the lead leakage in PSCs. A dormant acrylamide monomer induced into a perovskite film as an additive and being transformed into a chelating polymer network by applying heat. The network polyacrylamide in PSCs chelates and immobilizes lead ions. The unencapsulated devices for water-soluble lead concentration tests reveal that lead concentration in water can be reduced from 2.90 ppm for a control device to 0.74 ppm [22]. In addition, a high conductive metal-organic framework (MOF) with porous microstructure is deemed to be another candidate for capturing lead leakage in PSCs [23]. Yet, the priority for transporting layer or in situ additive in the perovskite layer is to effectively commute charge carriers, electrons, or holes. As a result, the thickness of such a transporting layer/additive is usually confined to tens of nanometers. The trade-off between capacity for lead-capturing and carrier communication of transporting layers is laborious to reach. On the other hand, the physical barrier for wrapping the PSCs is also developed to prevent their lead leakage. Self-healing resin encapsulation can physically decelerate water permeation into a device. That is, the water-soluble lead in PSCs is confined to a space between an impermeable glass-based substrate and a cover substrate. The only pathway for soluble lead is to penetrate the edge-sealing resin. However, this strategy can only slow down the process of lead leakage. Eventually, lead leaks out from devices [24].

As a result, reducing the lead content in PSCs is an important target for eliminating the concern about lead. Alkaline earth elements are deemed to be a suitable candidate for lead substitution owing to their stable divalent configuration and appropriate ionic radius. The criteria for substitutional conditions for a solid solution are based on the Hume-Rothery rules: the mismatch between two ionic radii should be lower than 15%; the valency of the candidate and its crystal structure should be the same as the original ion; the electronegativity should be as similar as possible between two ions [25, 26]. Considering compatibility between perovskite lattices, barium offers high flexibility for lead substitution compared to others [27]. The least crystal distortion supplies the highest photovoltaic performance for such PSCs. The cation engineering for extending the substituted tolerance of B-site cation further promotes the substitution ratio to 5.0 mol.% in mixed A-site cation PSCs with an improved PCE [28]. Polymer additives also stabilize the crystal structure as 5.0 mol.% lead is substituted with barium. By taking advantage of a uniform surface morphology and stable crystal structure, it is possible to achieve a power conversion efficiency greater than 16% from 10 mol.% barium-substituted PSCs [29]. The construction of a quasi-2D structure has been reported to enlarge the substitution ratio of B-site cations and effectively passivate defects in the perovskite layer. With 10 mol.% barium substitution, the PCE can exceed 19% [30]. However, very few studies have discussed the limit of substituting barium for lead.

In this study, beyond simply looking at the efficiency of PSCs, mixed A-site cation perovskite materials composed of methyl ammonium (MA) and formamidinium (FA) are investigated to determine the ceiling for lead replacement. The simple chemical composition of perovskite helps to reveal the limitations of lead reduction ratios. Based on surface potential and diffusion length analysis of barium-substituted perovskite, a 6 : 4 molar ratio FA/MA mixed A-site cation perovskite was chosen with a barium substitution ratio of 15 mol.%. The corresponding champion device retains a PCE of 11.13%, which is the highest record for 15 mol.% lead-reduced PSC. Further increases in the barium substitution ratio result in a rapid decrease in PCE, indicating that the ceiling for barium substitution ratio is 15 mol.% in FA/MA mixed A-cation PSCs.

2. Experimental Section

2.1. Preparation of Precursor. All chemicals are used as received without further purification. For precursor solution preparation, $MA_{0.4}FA_{0.6}Ba_xPb_{1-x}I_yCl_{3-y}$ is prepared by dissolving the desired ratio of CH_3NH_3I (MAI, FrontMaterials)/CH_5IN_2 (FAI, FrontMaterials), lead iodide (PbI_2, 99.9985%, Alfa Aesar)/lead chloride ($PbCl_2$, 99.999%, Sigma-Aldrich) (molar *ratio* = 0.9/0.1) in a mixture solvent (1 : 1 *v*/*v*) of dimethyl sulfoxide (DMSO, 99.9%, ECHO), and γ-butyrolactone (GBL, ≥99%, Sigma-Aldrich) at 40°C with continuous stirring for 24 h. For barium-substituted perovskite, barium iodide (BaI_2, 99.995%, Sigma-Aldrich) with various doping concentrations is used to substitute lead into perovskite precursor solution. The TiO_2 precursor solution for the compact layer and the paste for the mesoporous zinc-doped TiO_2 electron transport layer are synthesized and prepared based on previous studies [27, 31]. The hole transport layer solution contains 80 mg spiro-OMeTAD (FrontMaterials), 28.5 μL 4-tert-butylpyridine (tBP, 96%, Sigma-Aldrich), 17.5 μL Li-TFSI solution (Li-TFSI, 99.95%, Sigma-Aldrich, 1.8 M in acetonitrile), and 1.0 mL chlorobenzene (C6H5Cl, CB, 99.8%, ACROS). The mixture is stirred for 30 min until spiro-OMeTAD is completely dissolved. The solutions are all prepared in a nitrogen-filled humidity box (~1.0% relative humidity, 25°C).

2.2. Fabrication of Perovskite Solar Cell. Before device fabrication, FTO substrates (7 Ω, Ruilong) are cleaned in a sequential sonication step in the order of detergent, acetone, and isopropanol. Each step lasts 30 min to remove an adsorbed organic contaminant. Then, the FTO substrates

are modified using a UV-ozone cleaner to make their surface more hydrophilic. A dense TiO_2 layer is deposited onto the FTO substrate by spray coating and calcining at 450°C for 30 min. A mesoporous electron-transporting layer, zinc-doped TiO_2, is screen-printed onto the dense TiO_2 layer and calcined at 500°C for 30 minutes. The perovskite precursor solution, $FA_xMA_{1-x}Pb_{0.85}Ba_{0.15}I_yCl_{3-y}$ or other perovskites, is spin-coated onto the as-prepared electron transport layer by a two-step process with the first step at 1000 rpm and the second step at 5000 rpm for 20 sec, respectively. An antisolvent of 300 μL chlorobenzene is dripped onto the top of the perovskite film with 3 seconds remaining. After spin-coating, the perovskite film is transferred onto a hot plate and annealed at 100°C for 10 minutes. After cooling to room temperature, a hole transport layer of spiro-OMeTAD is deposited onto the perovskite film by the spin-coating process at 4000 rpm for 30 sec. Twelve silver electrodes with an area of 0.09 cm^2, confined by a metal mask, are thermal-evaporated onto the hole transport layer with a thickness of 120 nm. All processes regarding to spin-coating steps are carried out in a humidity box (~1.0% relative humidity, 25°C).

2.3. Characterization. The film topologies are acquired from field-emission scanning microscopy (FE-SEM, SU8010, Hitachi) and atomic force microscopy (AFM, Dimension-3100 Multimode, Digital Instruments) in the tapping mode. Optical properties are acquired by UV–vis spectrometer in the 600–1000 nm (V-730 Jasco). The crystal structure evolution of perovskite films is characterized by an X-ray diffractometer equipped with cross-beam optics (Rikagu SmartLab, 220C212). The surface potential is obtained from a Kelvin probe analyzer equipped with a 2 mm gold tip (SKP 5050, KP Technology) and a green 300 mW LED light source. The carrier dynamic analysis is acquired by a time-resolved photoluminescence spectrum (TR-PL, UniDRON-plus, UniNano Tech) with a 532 nm diode laser (LDH-D-TA-530, PicoQuant). Briefly, a perovskite film is deposited onto a quartz substrate and covered with a hole transport material of spiro-OMeTAD. In contrast, a perovskite film is deposited onto another substrate and covered by an electron transport layer of PC61BM. For reference, the intrinsic lifetime of perovskite film is deposited onto the same substrate and covered with an insulated layer of PMMA. The carrier lifetime of electron and hole in perovskite film can be thereafter derived from 1D approximation. In terms of electron trap density and electron mobility, a J-V curve from an electron-only device exhibiting FTO/TiO_2/perovskite/PC61BM/Ag architecture is measured and fitted with the space charge limit current model. All J-V curves in this study are recorded by a digital source meter (Keithley 2400) with a delay time of 200 ms. The light source for photovoltaic performance estimation is calibrated to 1 sun (AM 1.5G, 100 mW/cm^2) with a KG5-filtered silicon reference cell (BS-520BK, Bunkokeiki).

3. Results and Discussion

To enhance the crystal structure tolerance for barium substitution, formamidinium, which has a large ionic radius, is induced to comprise a mixed-cation perovskite. Figure 1 demonstrates the surface morphology of perovskite films composed of various chemical compositions, $FA_xMA_{1-x}Pb_{0.85}Ba_{0.15}I_{3-y}Cl_y$, where x varies from 0.0 to 0.8 ($FA_xMA_{1-x}Pb_{0.85}Ba_{0.15}I_{3-y}Cl_y$ perovskite is defined as Ba-PVK-x for further discussion). Different from conventional triiodide perovskite, we adopt a slight dopant of chloride, $x = 0.1$, to improve the film morphology and to fit the octahedron and Goldschmidt tolerance factor of crystal structure with small cationic radii. Based on the FE-SEM images in Figures 1(a)–1(e) series, the domain sizes of Ba-PVK-x evolve as the ratio of formamidinium, the x value, increases. The pin-hole density decreases as the ratio of formamidinium increases. This can be attributed to the merging of Ba-PVK-x domains, which occurs with an increased formamidinium ratio. The film coverage of these films is calculated and summarized in Table S1. Without a doubt, the film coverage increases to 99.8% when the formamidinium ratio reaches 0.8. High film coverage is expected to result in an ideal film-stacking scenario for subsequent layers. The surface roughness obtained from atomic force microscopy (Figures 1(f)–1(j)) is also analyzed and summarized in Table S1. The surface roughness initially decreases to an Rms value of 47.5 nm when x reaches 0.6. However, it subsequently increases, leading to a high surface roughness of 67.5 nm when x reaches 0.8. The mismatch in ionic size between the A-site and B-site cations results in noticeable aggregation effects of colloids and a large hydrodynamic diameter in a precursor solution [32]. A precursor with a large hydrodynamic diameter promotes rapid grain growth but results in small grain sizes. On the other hand, a precursor with a small hydrodynamic diameter leads to slow crystallization and the formation of larger grain sizes. Furthermore, a high ratio of formamidinium in perovskite expands the tolerance for barium substitution from the octahedral and tolerance factors point of view. This suggests that perovskite with a high x value would have a small hydrodynamic radius in the precursor, leading to larger grain sizes, as observed in topographic microscopies. In addition to the x value, chloride in perovskite not only promotes film coverage but also enhances the tolerance of the Ba substitution ratio regarding to octahedron and Goldschmidt tolerance factor [27, 33]. However, chloride is known as a volatile ion. It tends to vanish away from the film during the thermal annealing process that deteriorates the balance of stoichiometry between cation and anion in the perovskite structure. As a result, we adopt 10 mol.% of chloride incorporation ratio, namely, $y = 0.1$, for further discussion.

Besides the morphology effect, the chemical composition of perovskite plays an influential role in its energy bandgap. Figure 2 shows the optical properties of perovskite with various cation compositions, x from 0.0 to 0.8. As shown in Figure 2(a), the absorption edge redshifts as the x value increases. All energy bandgaps for perovskite films are determined from the corresponding Tauc plot, as shown in Figure 2(b). The redshift of the energy bandgap from 1.58 eV for Ba-PVK-0.0 to 1.52 eV for Ba-PVK-0.8 mainly comes from the lattice evolution as the large cation ratio increases. The lattice structure evolution of perovskite has

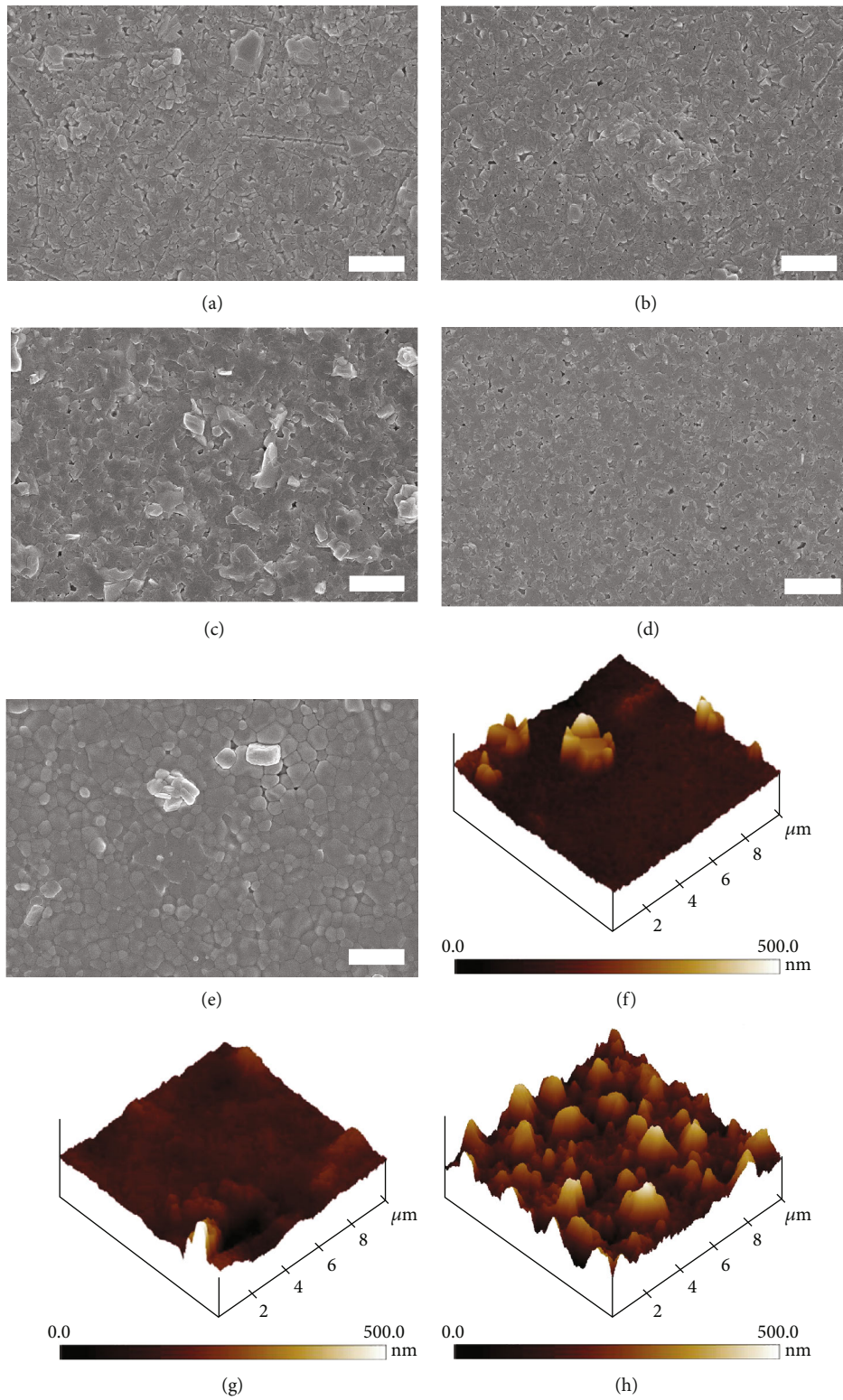

Figure 1: Continued.

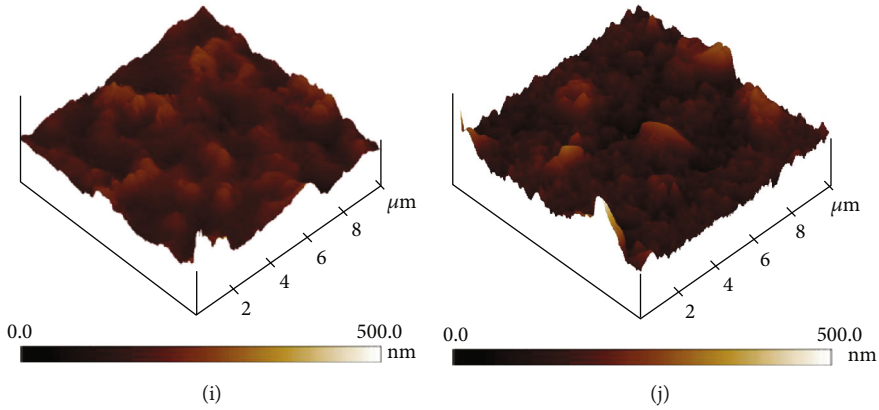

FIGURE 1: Morphology and the corresponding topography of $FA_xMA_{1-x}Pb_{0.85}Ba_{0.15}I_{3-y}Cl_y$ film: (a, f) $x = 0.0$, (b, g) $x = 0.2$, (c, h) $x = 0.4$, (d, i) $x = 0.6$, and (e, j) $x = 0.8$. (a–e) Morphology acquired from FE-SEM at a magnification of 30,000 and (f–j) topography from AFM (The scale bar indicates 2.0 μm in FE-SEM images).

been reported to affect the energy bandgap through different degrees of overlapping electrons in the p orbital from halide and cations [34]. In addition, the absorption spectrum for $x = 0.8$ appears to be different compared to the others. The decreased absorption in the visible light band can be ascribed to the phase transition of formamidinium perovskite. As a photoactive phase yet unstable perovskite, α-phase formamidinium lead triiodide gradually transitions to a yellow phase metastable δ-phase at room temperature. It results in a decrease in light absorption ability.

To gain insight into the speculation above, the crystal structures of the films were analyzed by X-ray diffractometer, and the results are shown in Figure 3(a). Owing to the high crystallinity of perovskite in the out-of-plane direction, the {110} facets can be observed in all films with various chemical compositions. The characteristic peaks at 26.5, 33.7, 37.8, and 51.6° refer to FTO substrates. Different from the other films, the Ba-PVK-0.8 shows a pronounced δ-phase $FAPbI_3$ at 11.8°. The expended patterns from 13° to 15° and 27° to 29° provide insights into the crystal structure evolution with increasing x value (Figures 3(b) and 3(c)). As a large cation, inducing a large A-site cation of formamidinium causes a noticeable lattice expansion of the perovskite. Obvious peak shifts from 14.1° of facet (110) toward 13.9° and 28.4° of facet (220) toward 28.1° are observed. In addition, splitting peaks are observed at low concentrations of formamdinium composition ($x < 0.4$) that indicates the mismatch of edges for a tetragonal lattice structure, where the lattice parameters are unequal ($a = b \neq c$). High concentrations of formamidinium composition ($x \geq 0.4$) exhibit single peaks at both positions. It indicates the lattice parameters reaching a balance ($a = b = c$) as the crystal structure turns from tetragonal to cubic.

The X-ray absorption near the edge structure (XANES) and the extended X-ray absorption fine structure (EXAFS) of the lead in Ba-PVK-x, x from 0.0 to 0.8, are also investigated to reveal its oxidation state and geometric information, namely, the distance between lead and proximate ion. Figure S1 (a) illustrates the Pb K-edge of Ba-PVK-x. The steady XANES indicates the oxidation state of lead is stable. That is, the incorporation of formamidinium shows minor interference in the oxidation state of lead in the perovskite structure. The real space distance reduction can be observed from EXAFS and is plotted in Figure S1 (b). Based on the perovskite lattice structure, iodide is the neighboring ion of lead, which bonds together and constructs PbI_6 octahedrons. The distance in Ba-PVK-0.0 shows a slightly longer distance. The large electronegativity of barium tends to attract the neighboring iodide and results in the slight expansion of the adjacent PbI_6 octahedron. As formamidinium ions are induced into such perovskite structures, the relatively large A-site cations are speculated to alleviate the expansion effect of PbI_6 octahedrons caused by the neighboring barium ions. As a result, the distance between lead ion and iodide shifts to a smaller value, which is almost the same as perovskite with methylammonium lead iodide perovskite, Ba-PVk-0.0. The similar distance of Ba-PVK-x for x from 0.2 to 0.8 reveals that the barium substitution into perovskite structure barely interferes with the formation of octahedrons of PbI_6. As such, a perovskite with a stable crystal structure can be rationally implied. The preliminary tests for their PV performance are conducted to show the correlation of photovoltaic performance between film properties after various ratios of large cation incorporation. The PCE distributions acquired from Ba-PVK-x devices with various compositions, x from 0.0 to 0.8, are shown in Figure 4(a). It underscores the pronounced impact of formamidinium incorporation on the enlargement effect for barium substitution, as evidenced by the enhancement in photovoltaic performance. Yet, when focusing on Ba-PVK-0.8, it highlights that incorporating an excessive amount of formamidinium can have a detrimental effect on the photovoltaic performance due to the rapid increase of the δ-phase $FAPbI_3$ in the film (see Figure 3). Note that δ-phase $FAPbI_3$ is widely known as a photoinactive phase perovskite structure. The corresponding film absorption in the visible light region also shows a dramatic drop owing to the formation of δ-phase $FAPbI_3$. Among them, the devices with Ba-PVK-0.6 perovskite stand out with an average PCE of 10.30%. The J-V curves of champion devices are shown in Figure 4(b). It achieves a PCE of

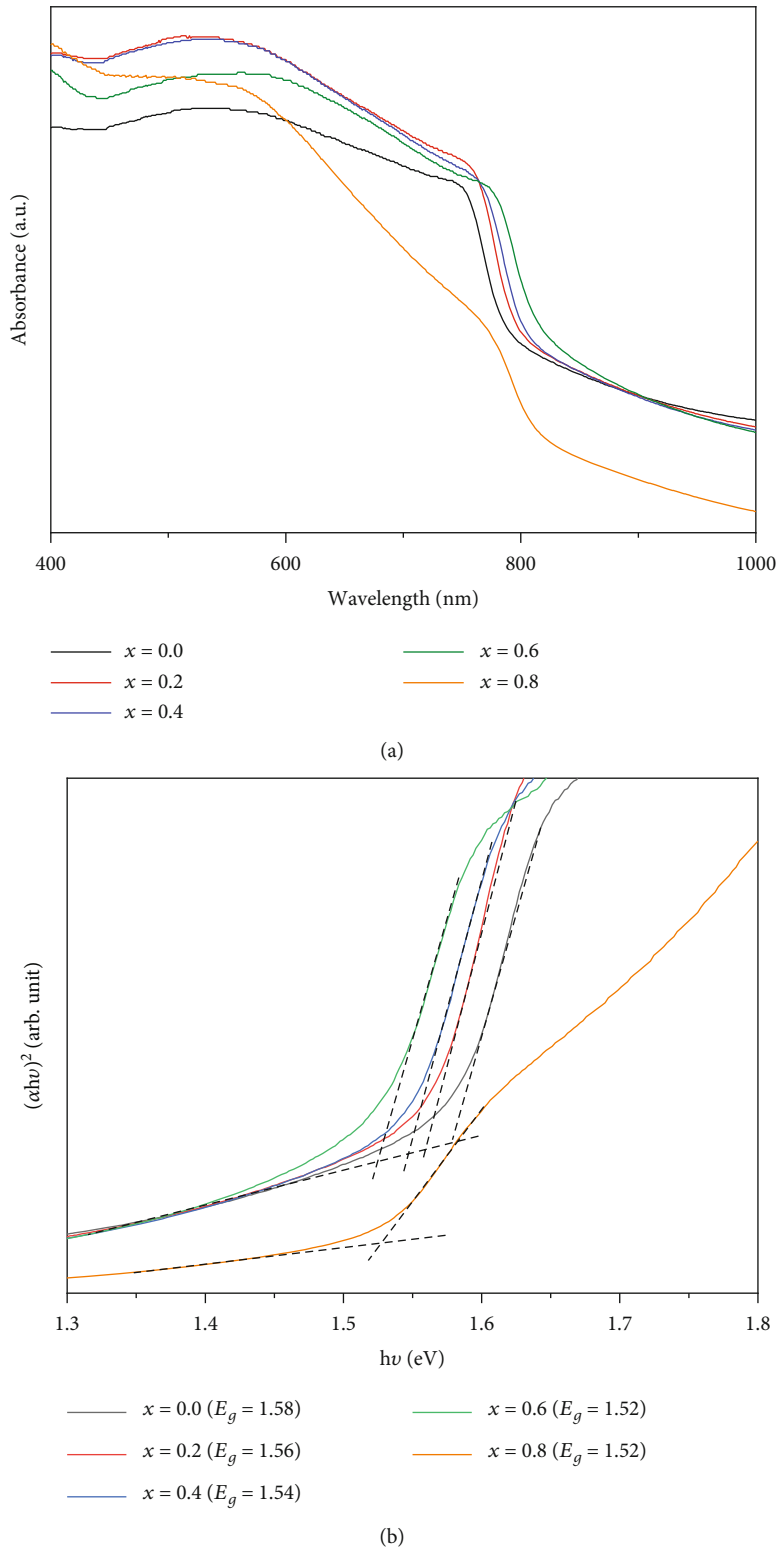

FIGURE 2: Optical property of $FA_xMA_{1-x}Pb_{0.85}Ba_{0.15}I_{3-y}Cl_y$ film: (a) absorption spectrum and (b) corresponding Tauc plot for energy bandgap calculation.

11.13% with an open-circuit voltage (V_{OC}) of 1.05 V, a short-circuit current (J_{SC}) of 16.03 mA/cm^2, and a fill factor of 66.06%. The lowest energy bandgap of perovskite film reflects on its highest current density in the series. The tremendous difference in the PV performance between the Ba-PVK-0.0 and Ba-PVK-0.6 devices inspires us to dig into the influence of barium compatibility with the assistance of large A-site cations. When focusing on the enhancement of

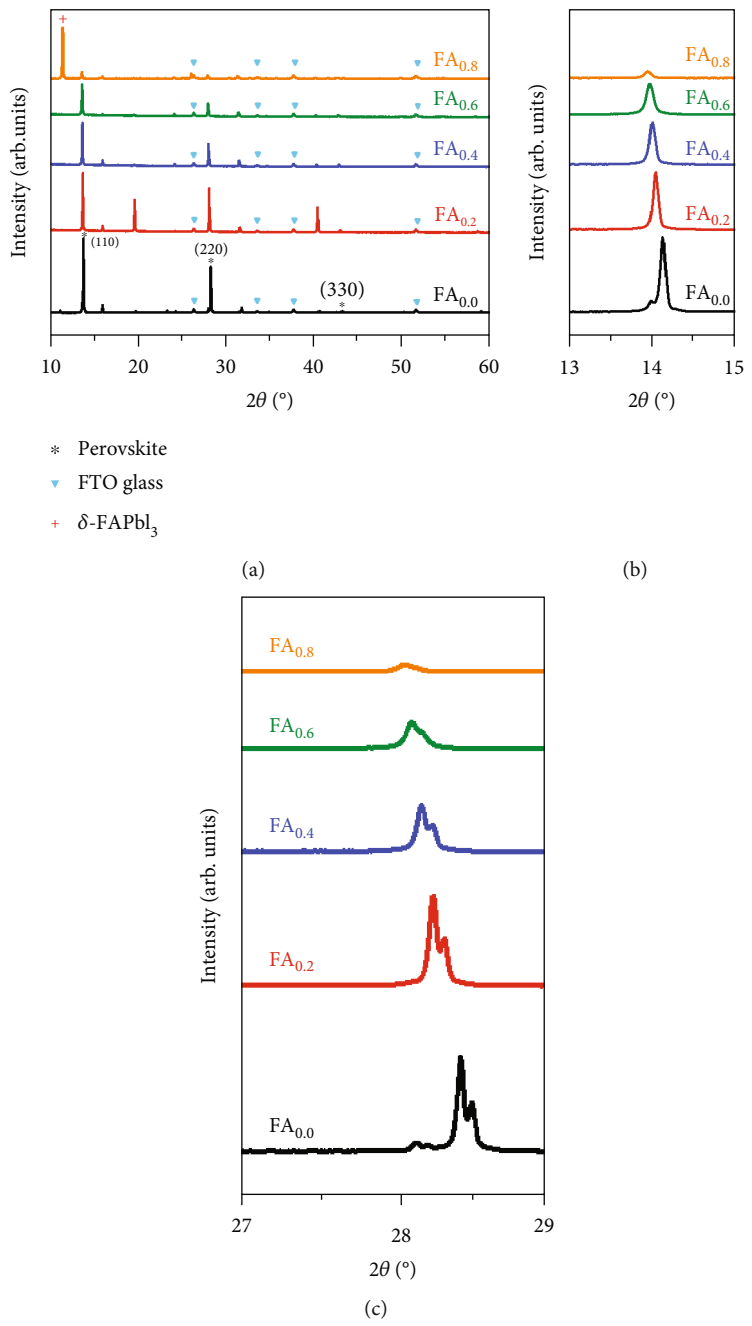

FIGURE 3: Crystal structure analysis of $FA_xMA_{1-x}Pb_{0.85}Ba_{0.15}I_{3-y}Cl_y$ film, x from 0.0 to 0.8: (a) full range X-ray diffraction pattern, (b) expansion pattern from 13° to 15, and (c) expansion pattern from 27° to 29°.

the PV performance, the V_{OC} of PV devices is highly relative to the intrinsic properties, namely, the potential difference between interfaces, of the comprised materials. To further investigate the effect of barium on potential change, photo-assisted Kelvin probe microscopy (photo-KPFM) is adopted to examine the potential evolution as the films are exposed to intermittent light (red light with a peak position at 656 nm). Figure 4(c) shows the potential evolution of Ba-PVK-0.0 and Ba-PVK-0.6 films deposited onto a silicon substrate. As light strikes the films, the contact potential shifts to high potential. The upshift of contact potential is indicative of excited electrons that are generated, which prefer to stay at the surface of the films. The difference between starting points is ascribed to the energy level difference between Ba-PVK-0.0 and Ba-PVK-0.6 films. The different degree of shifting potential implies the different densities of excited electrons at the surface of perovskite films. The upshift of potential also refers to the decreasing work function as light strikes. On the other hand, the contact potential shifts in the opposite direction for Ba-PVK-0.0 and Ba-PVK-0.6 deposited onto an electron transport layer of the TiO_2 layer. Due to the built-in potential at the interface between the Ba-PVK-0.0/Ba-PVK-0.6 layer and the TiO_2 layer, the excited electrons are

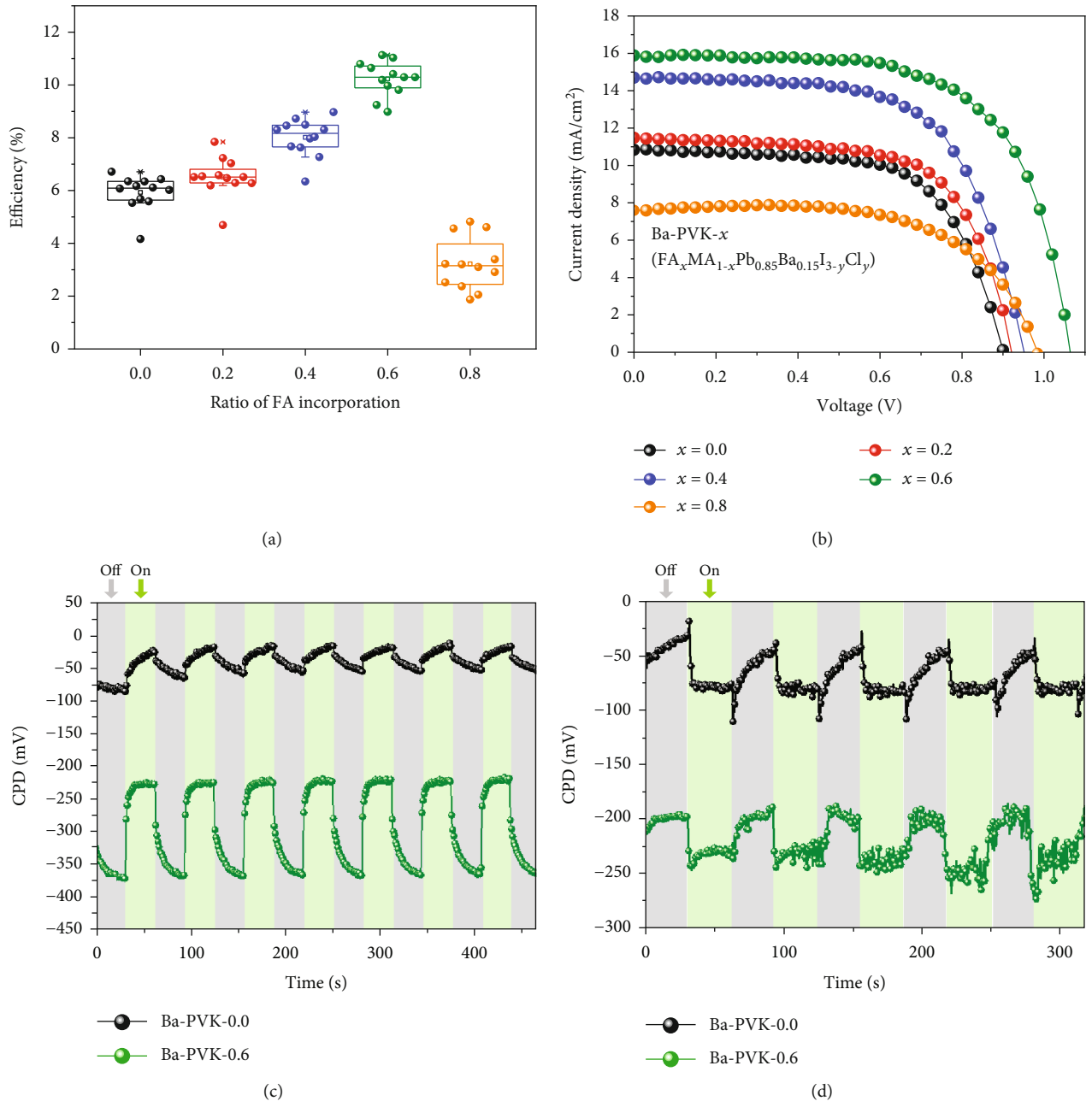

FIGURE 4: Photovoltaic performance analysis for $FA_xMA_{1-x}Pb_{0.85}Ba_{0.15}I_{3-y}Cl_y$: (a) PCE distribution for 12 individual devices and (b) J-V curves of corresponding champion devices (x from 0.0 to 0.8). Surface potential evolution for $x = 0.0$ and $x = 0.60$: (c) surface potential analysis for films deposited onto a silicon wafer and (d) the films deposited onto an electron transporting layer.

driven toward the TiO_2 layer and separating electron-hole pairs. As a result, the excited holes prefer to stay at the surface of Ba-PVK-0.0/Ba-PVK-0.6 in both cases. Note that the leaving number of holes at the surface of films is proportional to the surface potential change (ΔCPD). The positive charge of holes makes CPD change in the opposite direction as compared to the effect of accumulated electrons at their surface. The results in reverse tendency in terms of potential change are shown in Figure 4(d). The consistently large potential difference between Ba-PVK-0.0 and Ba-PVK-0.6 at both conditions reveals the minor defects in the Ba-PVK-0.6 perovskite layer. Therefore, it can create a pronounced potential difference as light strikes it. This is beneficial to gain both high photocurrent and voltage as the film acts as an active layer in a PSC (refer to Figure 4(b)).

To validate the speculation, the carrier dynamic is studied to demonstrate the carrier diffusion lengths in both Ba-PVK-0.0 and Ba-PVK-0.6 layers. The Ba-PVK-0.0 and Ba-PVK-0.6 films are deposited onto a quartz substrate and covered with either a carrier transport layer or an insulated layer (for details, see *Experimental Section*). Steady-state

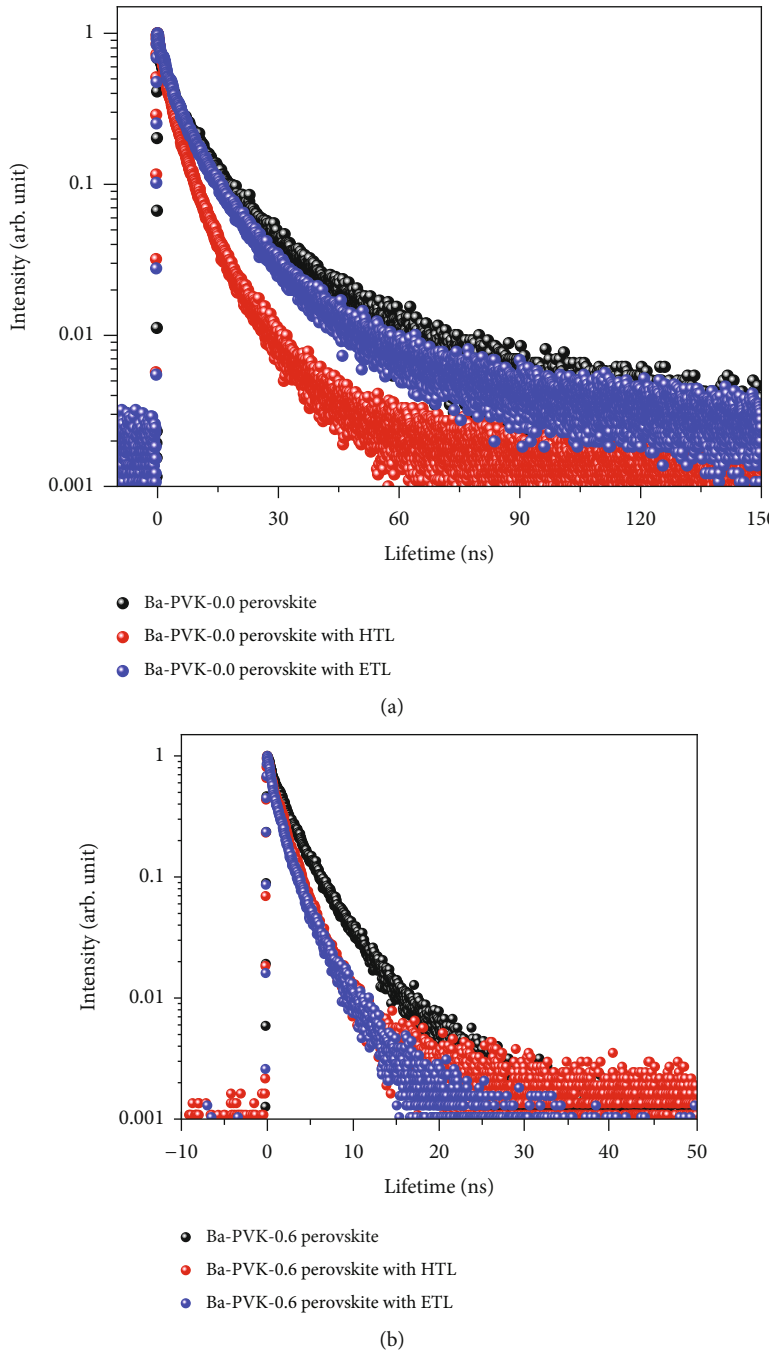

Figure 5: Carrier dynamic analysis of control and target perovskite: (a) time-resolved photoluminescence spectra for Ba-PVK-0.0 and (b) time-resolved photoluminescence spectra for Ba-PVK-0.6.

photoluminescence spectra (PL spectra) are first measured to observe the carrier recombination behavior. The redshift of PL spectra for Ba-PVK-0.6 compared to Ba-PVK-0.0 again reveals the energy bandgap decreasing as a large A-site cation is induced into perovskite material, as shown in Figure S2 (a), that is consistent with the absorption spectra in Figure 2. In addition, the high PL intensity demonstrates inferior nonradiative recombination in Ba-PVK-0.6 than in Ba-PVK-0.0. The dramatic reduction of PL intensity in Figure S2 (b) and (c) reveals that the carrier transfer in Ba-PVK-0.6 is much more pronounced than Ba-PVK-0.0 owing to its minor nonradiative recombination. Figures 5(a) and 5(b) show time-resolved photoluminescence spectra (TR-PL) for Ba-PVK-0.0 and Ba-PVK-0.6 layers. With the assistance of a quenching layer, the carrier decay time decreases in both Ba-PVK-0.0 and Ba-PVK-0.6 films. As discussing carriers in a perovskite solar cell, their diffusion occurs under the trigger of potential difference in such a device. That confines carriers to migrate along with the (opposite) direction of built-in potential. The carrier diffusion length

Table 1: Charged carrier dynamic and corresponding diffusion length.

	Thickness (nm)	τ_{PMMA} (ns)	τ_{PCBM} (ns)	τ_{Spiro} (ns)	L_D (nm), e^-	L_D (nm), h^+
Ba-PVK-0.0	550	7.27	4.07	6.36	187	439
Ba-PVK-0.6	560	2.61	1.62	1.48	395	440

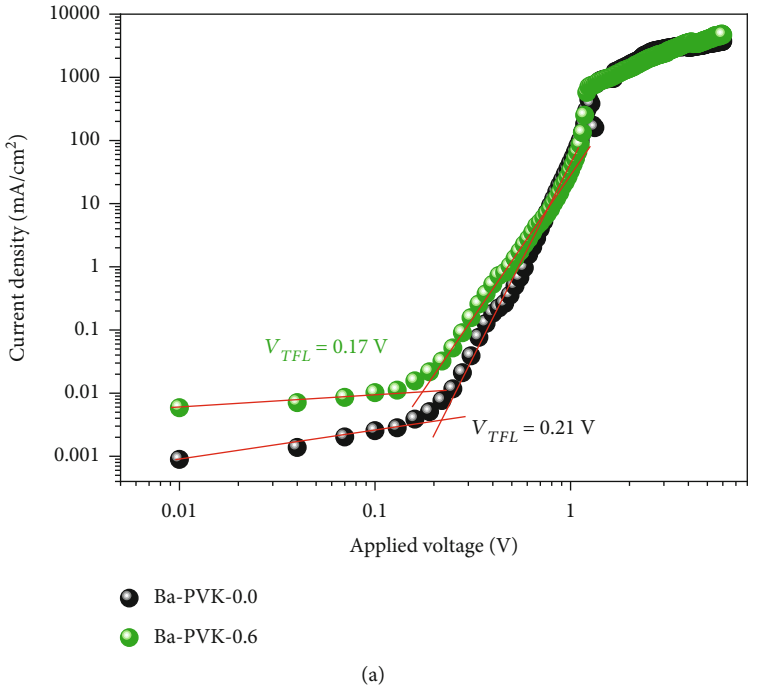

(a)

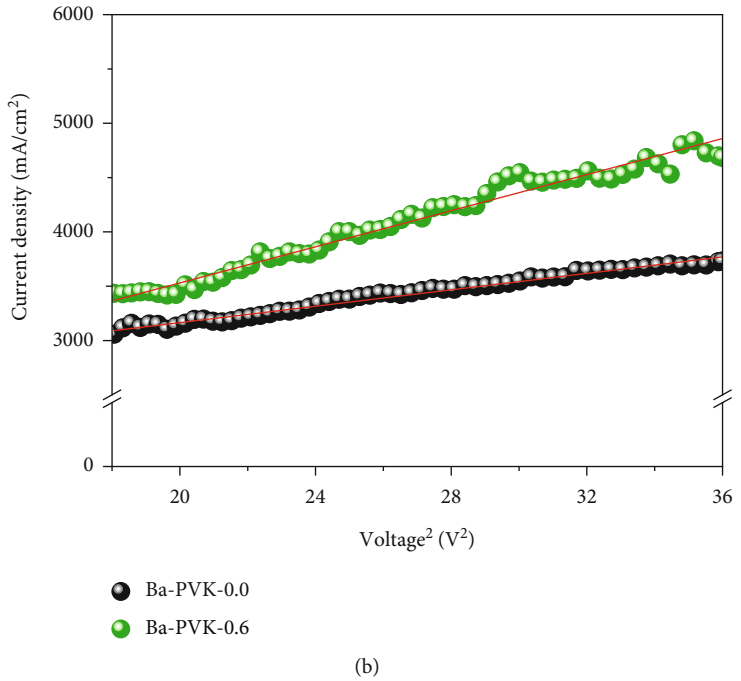

(b)

Figure 6: Electron-only devices for space charge limit current model fitting: (a) J-V curve from applied bias from 0.01 to 6.00 V and (b) electron mobility estimation in child's region.

Table 2: Summarized electron trap density and electron mobility from the J-V curves of electron-only devices.

	Thickness (nm)	V_{TFL} (V)	Electron trapped density (#/cm^3)	Electron mobility (cm^2/(V·s))
Ba-PVK-0.0	550	0.21	2.46×10^{15}	1.98
Ba-PVK-0.6	560	0.17	1.92×10^{15}	4.57

Table 3: State-of-the-art lead-reduced perovskite with alkaline earth element substitution.

Substituent	Substituent ratio (at. %)	Perovskite composition	V_{OC} (V)	J_{SC} (mA/cm^2)	FF (%)	PCE (%)	Reference
Ba	10.0	$FA_{0.60}MA_{0.40}Pb_{0.90}Ba_{0.10}I_{3-x}Cl_x$	1.08	21.47	68.11	15.85	This work
Ba	15.0	$FA_{0.60}MA_{0.40}Pb_{0.85}Ba_{0.15}I_{3-x}Cl_x$	1.06	16.03	65.21	11.13	
Mg	1.0	$MAPb_{0.99}Mg_{0.01}I_{3-x}Cl_x$	0.94	15.30	57.40	8.30	[37]
Ca	1.0	$MAPb_{0.99}Ca_{0.01}I_{3-x}Cl_x$	0.98	19.10	68.40	12.90	[38]
Ca	5.0	$CsPb_{0.95}Ca_{0.05}I_3$	0.95	17.90	80.00	13.50	[39]
Sr	1.0	$MAPb_{0.99}Sr_{0.01}I_{3-x}Cl_x$	0.90	18.90	62.60	10.60	[37]
Sr	2.0	$CsPb_{0.98}Sr_{0.02}I_2Br$	1.04	15.30	69.90	11.20	[40]
Sr	5.0	$MAPbI_3$	1.11	21.08	71.00	16.30	[41]
Sr	5.0	$MAPbI_3$	1.02	19.96	75.00	16.08	[42]
Sr	10.0	$MAPbI_3$	1.08	19.45	74.00	15.64	[43]
Ba	1.0	$MAPb_{0.99}Ba_{0.01}I_{3-x}Cl_x$	0.93	20.20	65.60	12.30	[37]
Ba	3.0	$MAPb_{0.97}Ba_{0.03}I_{3-x}Cl_x$	0.99	20.40	69.60	14.90	[27]
Ba	10.0	$MAPb_{0.80}Ba_{0.10}I_{3-x}Cl_x$	0.85	18.80	60.40	9.70	[31]
Ba	10.0	$PEG\text{-}FA_{0.6}MA_{0.4}Pb_{0.9}Ba_{0.1}I_{3-x}Cl_x$	1.06	22.90	66.80	16.10	[29]
Ba	10.0	$PEA_{0.01}FA_{0.60}MA_{0.39}Pb_{0.90}Ba_{0.10}I_{3-x}Cl_x$	1.14	23.20	72.00	19.10	[30]

of electron and hole in Ba-PVK-0.0 and Ba-PVK-0.6 film can be thereafter derived from 1D approximation as expressed in the following equation [35, 36]:

$$L_D = \frac{2d}{\pi}\sqrt{2\left(\frac{\tau}{\tau_{\text{quench}}} - 1\right)}. \quad (1)$$

Here, L_D is the carrier diffusion length, d is the film thickness, τ is the carrier lifetime, and τ_{quench} is the carrier lifetime with a quenching layer. The calculated carrier diffusion lengths (L_D) in both types of films are summarized in Table 1. Sharing the same preparation steps, the thicknesses of the films are almost the same at 550 nm, as shown in Figure S3. Because of the ambipolar nature, the diffusion lengths of holes and electrons in a perovskite film have similar diffusion lengths. Based on the charged carrier dynamic analysis, Ba-PVK-0.0 has an electron diffusion length of 187 nm, less than half of its hole diffusion length of 439 nm. In contrast, Ba-PVK-0.6 exhibits a much similar electron diffusion length of 395 nm and hole diffusion length of 440 nm. This can be ascribed to the different compatibility of barium substitution between mono A-site cation and mixed A-site cation perovskite structures. With the introduction of a large cation, formamidinium, into the perovskite structure, barium substitution becomes feasible due to a favorable aspect of tolerance or octahedral factor. Furthermore, the excess barium ions in perovskite might form uncoordinated ions or interstitial defects. Both are regarded as cationic defects and annihilate the negatively charged electrons through a defect-assisted recombination process. The relatively high probability of such a recombination route results in a short electron diffusion length in Ba-PVK-0.0 compared to that of Ba-PVK-0.6. From the charged carrier collection point of view, the perovskite film thickness should be as close as possible to the calculated diffusion length of both electrons and holes. Losing balance between electron and hole diffusion length hinders effective electrons and hole transfer from perovskite layers to electrodes. As a result, the drawback of barium substitution in Ba-PVK-0.0 is directly reflected in the decrease of photocurrent, as mentioned in Figure 4(b).

To confirm the as-mentioned scenario, the J-V curve from Ba-PVK-0.0 and Ba-PVK-0.6 electron-only devices are characterized to reveal their electron trap density and corresponding electron mobility as shown in Figures 6(a) and 6(b). Based on the space-charge limit current (SCLC) model, a J-V curve from an electron-only device can be divided into three portions, Ohmic region, trap-filled region, and child's region. The onset point (V_{TFL}) between the Ohmic region and trap-filled region offers information about electron trap density, whereas the slope in the child's region provides information about electron mobility. The electron trap density and electron mobility of a film can be derived by the following:

$$V_{TFL} = \frac{eN_t d^2}{2\varepsilon\varepsilon_0}, \qquad J = \frac{9\varepsilon\varepsilon_0\mu V^2}{8d^3}. \quad (2)$$

Here, e represents the elementary charge, ε and ε_0 are the dielectric permittivity constants of perovskite and the vacuum, N_t is the electron-trapped density of a film, d is the thickness of a perovskite film, and μ is the electron mobility of a film. The results from the SCLC model fitting are summarized in Table 2. The calculated electron-trapped density from V_{TFL} decreases from 2.46×10^{15} for Ba-PVK-0.0 to 1.92×10^{15} for Ba-PVK-0.6. Additionally, electron mobility improves to 4.57 $cm^2/(V{\cdot}s)$ in Ba-PVK-0.6 compared to 1.98 $cm^2/(V{\cdot}s)$ in Ba-PVK-0.0. The electron-trapped density decrease and electron mobility improvement originated from the fewer positive defects, namely, uncoordinated Ba^{2+}, in Ba-PVK-0.6 films. The fewer positive defects a film has, the less probability of electron annihilation occurs as electron communication along with the applied bias results in high electron mobility.

Figure S4 reveals the correlation between further barium substitution of lead and their PCE in mixed A-site cation perovskite solar cells. The PCE distribution of barium-substituted perovskite solar cells infers that the PCE from barium-substituted perovskite can retain over 90% of PCE as barium-substituted ratio lower than 10 mol.%. For 15 mol.% of barium-substituted perovskite solar cells, the average PCE can maintain over 60% of mixed A-site perovskite solar cells. The further substitution of lead, 20 mol.% of barium-substituted perovskite, makes a deterioration of the PCE and remains only 19% of PCE compared to lead-based composition, $FA_{0.6}MA_{0.4}PbI_{3-y}Cl_y$. Table 3 summarizes the state-of-the-art lead-reduced perovskite solar cells. Among alkaline earth elements, barium delivers the highest PCE when it serves as a substituent element for lead in perovskite materials, which can achieve a PCE of 15.85% for 10 mol.% barium substitution and 11.13% for 15 mol.% of barium substitution.

4. Conclusion

Lead content in perovskite solar cells becomes an eye-catching issue as such photovoltaics have made great progress recently. Herein, systematic analyses, including morphology, crystal structure, optical property, and carrier dynamic, have been studied to reveal the correlation between tolerance of barium substitution and A-site cation composition. The high barium substitution ratio of 15 mol.% can be achieved when inducing 60 mol.% of a large A-site cation, formamidinium, into the methylammonium perovskite. The induction of a large A-site cation into barium-substituted perovskite overcomes the imbalance between hole and electron diffusion lengths, resulting in an electron and a hole diffusion length of 395 nm and 440 nm, respectively. The champion device for 15 mol.% barium substituted perovskite, $FA_{0.6}MA_{0.4}Pb_{0.85}Ba_{0.15}I_{3-y}Cl_y$, achieves a PCE of 11.13%, which is the highest record for 15 mol.% of lead reduction. However, any further substitution of lead (>20 mol.%) results in a dramatic decrease in PCE. This study points out that the ceiling for the barium-substituted ratio is about 15 mol.% in such mixed cation perovskite.

Data Availability

The authors confirm that the data supporting the findings of this study are available within the article and/or its supplementary materials.

Conflicts of Interest

The authors declare that they have no conflicts of interest.

Authors' Contributions

Kai-Chi Hsiao and Ching-Mei Ho contributed equally to this work.

Acknowledgments

The authors appreciate Dr. Ming-Tao Lee (BL-13A1), Dr. Jyh-Fu Lee (BL-17C1), and Dr. Ting-Shan Chan (BL-01C1) at the National Synchrotron Radiation Research Centre for their useful discussion and suggestions and Mr. Y.-S. Chen at Instrumentation Centre of National Tsing Hua University for TEM analysis. The authors also thank the Microscopy Center at Chang Gung University for technical assistance. The financial support from the National Science and Technology Council, Taiwan (Project Nos. 108-2218-E-035-015-MY2, 110-2221-E-035-026, 111-2221-E-035-006, 111-2628-E-182-001-MY2, 111-2221-E-182-040-MY3, 112-2628-E-131-001-MY4, and 112-2221-E-035-004), Chang Gung University (URRPD2N0011), and Chang Gung Memorial Hospital at Linkou (CMRPD2N0061 and BMRPC74) are highly appreciated.

Supplementary Materials

Supplementary material for this article is available on the journal's online library. The supplementary material includes the following: X-ray absorption spectra of $FA_xMA_{1-x}Pb_{0.85}Ba_{0.15}I_{3-y}Cl_y$ films, photoluminescence spectrum of Ba-PVK-0.0 and Ba-PVK-0.6 covered with a quench layer or an insulated layer, device structure and cross-sectional FE-SEM, photovoltaic performance for devices with various ratios of barium substitution, and a summarized calculated film coverage and surface roughness of perovskite with various ratios of formamidinium. *(Supplementary Materials)*

References

[1] M. Yang, Z. Li, M. O. Reese et al., "Perovskite ink with wide processing window for scalable high-efficiency solar cells," *Nature Energy*, vol. 2, no. 5, p. 17038, 2017.

[2] C. Liang, D. Zhao, P. Li et al., "Simultaneously boost diffusion length and stability of perovskite for high performance solar cells," *Nano Energy*, vol. 59, pp. 721–729, 2019.

[3] Y. Wang, Y. Zhang, P. Zhang, and W. Zhang, "High intrinsic carrier mobility and photon absorption in the perovskite $CH_3NH_3PbI_3$," *Physical Chemistry Chemical Physics*, vol. 17, no. 17, pp. 11516–11520, 2015.

[4] https://www.nrel.gov/pv/cell-efficiency.html.

[5] B. A. Rosales, M. P. Hanrahan, B. W. Boote, A. J. Rossini, E. A. Smith, and J. Vela, "Lead halide perovskites: challenges and opportunities in advanced synthesis and spectroscopy," *ACS Energy Letters*, vol. 2, no. 4, pp. 906–914, 2017.

[6] G. Schileo and G. Grancini, "Lead or no lead? Availability, toxicity, sustainability and environmental impact of lead-free perovskite solar cells," *Journal of Materials Chemistry C*, vol. 9, no. 1, pp. 67–76, 2021.

[7] J. Li, H.-L. Cao, W.-B. Jiao et al., "Biological impact of lead from halide perovskites reveals the risk of introducing a safe threshold," *Nature Communications*, vol. 11, no. 1, p. 310, 2020.

[8] J.-J. Cao, Y.-H. Lou, W.-F. Yang et al., "Multifunctional potassium thiocyanate interlayer for eco-friendly tin perovskite indoor and outdoor photovoltaics," *Chemical Engineering Journal*, vol. 433, article 133832, 2022.

[9] M. Chen, G. Kapil, L. Wang et al., "High performance wide bandgap lead-free perovskite solar cells by monolayer engineering," *Chemical Engineering Journal*, vol. 436, article 135196, 2022.

[10] X. Liu, T. Wu, X. Luo et al., "Lead-free perovskite solar cells with over 10% efficiency and size 1 cm2 enabled by solvent–crystallization regulation in a two-step deposition method," *ACS Energy Letters*, vol. 7, no. 1, pp. 425–431, 2022.

[11] W. Ke and M. G. Kanatzidis, "Prospects for low-toxicity lead-free perovskite solar cells," *Nature Communications*, vol. 10, no. 1, p. 965, 2019.

[12] T.-B. Song, T. Yokoyama, S. Aramaki, and M. G. Kanatzidis, "Performance enhancement of Lead-free tin-based perovskite solar cells with reducing atmosphere-assisted dispersible additive," *ACS Energy Letters*, vol. 2, no. 4, pp. 897–903, 2017.

[13] E. W.-G. Diau, E. Jokar, and M. Rameez, "Strategies to improve performance and stability for tin-based perovskite solar cells," *ACS Energy Letters*, vol. 4, no. 8, pp. 1930–1937, 2019.

[14] Y. Jia, Y. Zeng, X. Li, and L. Meng, "Effect of Sr substitution on the property and stability of CH3NH3SnI3perovskite: a first-principles investigation," *International Journal of Energy Research*, vol. 44, no. 7, pp. 5765–5778, 2020.

[15] V. J.-Y. Lim, A. M. Ulatowski, C. Kamaraki et al., "Air-degradation mechanisms in mixed lead-tin halide perovskites for solar cells," *Advanced Energy Materials*, vol. 13, no. 33, article 2200847, 2022.

[16] L. Lanzetta, T. Webb, N. Zibouche et al., "Degradation mechanism of hybrid tin-based perovskite solar cells and the critical role of tin (IV) iodide," *Nature Communications*, vol. 12, no. 1, p. 2853, 2021.

[17] M. Asghar, M. W. Iqbal, M. Manzoor et al., "A computational insight of the lead-free double perovskitesRb2AgSbCl6andRb2AgSbBr6for optoelectronic and thermoelectric applications," *International Journal of Energy Research*, vol. 46, no. 15, pp. 24273–24285, 2022.

[18] Q. Mahmood, M. Younas, M. G. B. Ashiq, S. M. Ramay, A. Mahmood, and H. M. Ghaithan, "First principle study of lead-free double perovskites halidesRb2Pd(Cl/Br)6for solar cells and renewable energy devices: a quantumDFT," *International Journal of Energy Research*, vol. 45, no. 10, pp. 14995–15004, 2021.

[19] K.-C. Hsiao, Y.-F. Yu, C.-M. Ho et al., "Doping engineering of carrier transporting layers for ambient-air-stable lead-free rudorffite solar cells prepared by thermal-assisted doctor blade coating," *Chemical Engineering Journal*, vol. 451, article 138807, 2023.

[20] Z. Zhang, Q. Sun, Y. Lu et al., "Hydrogenated $Cs_2AgBiBr_6$ for significantly improved efficiency of lead-free inorganic double perovskite solar cell," *Nature Communications*, vol. 13, no. 1, p. 3397, 2022.

[21] J. Lee, G.-W. Kim, M. Kim, S. A. Park, and T. Park, "Nonaromatic green-solvent-processable, dopant-free, and lead-capturable hole transport polymers in perovskite solar cells with high efficiency," *Advanced Energy Materials*, vol. 10, no. 8, article 1902662, 2020.

[22] B. Niu, H. Wu, J. Yin et al., "Mitigating the lead leakage of high-performance perovskite solar cells via in situ polymerized networks," *ACS Energy Letters*, vol. 6, no. 10, pp. 3443–3449, 2021.

[23] S. Wu, Z. Li, M.-Q. Li et al., "2D metal–organic framework for stable perovskite solar cells with minimized lead leakage," *Nature Nanotechnology*, vol. 15, no. 11, pp. 934–940, 2020.

[24] X. Xiao, M. Wang, S. Chen et al., "Lead-adsorbing ionogel-based encapsulation for impact-resistant, stable, and lead-safe perovskite modules," *Science Advances*, vol. 7, no. 44, article eabi8249, 2021.

[25] W. Hume-Rothery and H. M. Powell, "On the theory of superlattice structures in alloys," *Zeitschrift für Kristallographie-Crystalline Materials*, vol. 91, no. 1-6, pp. 23–47, 1935.

[26] W. Xiang, Z. Wang, D. J. Kubicki et al., "Ba-induced phase segregation and band gap reduction in mixed-halide inorganic perovskite solar cells," *Nature Communications*, vol. 10, no. 1, p. 4686, 2019.

[27] S.-H. Chan, M.-C. Wu, K.-M. Lee, W.-C. Chen, T.-H. Lin, and W.-F. Su, "Enhancing perovskite solar cell performance and stability by doping barium in methylammonium lead halide," *Journal of Materials Chemistry A*, vol. 5, no. 34, pp. 18044–18052, 2017.

[28] S.-H. Chan, M.-C. Wu, Y.-Y. Li, K.-M. Lee, Y.-F. Chen, and W.-F. Su, "Barium doping effect on the photovoltaic performance and stability of $MA_{0.4}FA_{0.6}Ba_xPb_{1-x}I_yCl_{3-y}$ perovskite solar cells," *Applied Surface Science*, vol. 521, article 146451, 2020.

[29] M.-C. Wu, Y.-Y. Li, S.-H. Chan, K.-M. Lee, and W.-F. Su, "Polymer additives for morphology control in high-performance lead-reduced perovskite solar cells," *Solar RRL*, vol. 4, no. 6, article 2000093, 2020.

[30] S.-H. Chan, Y.-H. Chang, M.-H. Jao et al., "High efficiency quasi-2D/3D Pb–Ba perovskite solar cells via phenethylammonium chloride addition," *Solar RRL*, vol. 6, no. 6, article 2101098, 2022.

[31] M.-C. Wu, W.-C. Chen, S.-H. Chan, and W.-F. Su, "The effect of strontium and barium doping on perovskite-structured energy materials for photovoltaic applications," *Applied Surface Science*, vol. 429, pp. 9–15, 2018.

[32] P. Boonmongkolras, D. Kim, E. M. Alhabshi, I. Gereige, and B. Shin, "Understanding effects of precursor solution aging in triple cation lead perovskite," *RSC Advances*, vol. 8, no. 38, pp. 21551–21557, 2018.

[33] H.-C. Liao, P. Guo, C.-P. Hsu et al., "Enhanced efficiency of hot-cast large-area planar perovskite solar cells/modules having controlled chloride incorporation," *Advanced Energy Materials*, vol. 7, no. 8, article 1601660, 2017.

[34] R. Prasanna, A. Gold-Parker, T. Leijtens et al., "Band gap tuning via lattice contraction and octahedral tilting in perovskite

materials for photovoltaics," *Journal of the American Chemical Society*, vol. 139, no. 32, pp. 11117–11124, 2017.

[35] A. H. Proppe, R. Quintero-Bermudez, H. Tan, O. Voznyy, S. O. Kelley, and E. H. Sargent, "Synthetic control over quantum well width distribution and carrier migration in low-dimensional perovskite photovoltaics," *Journal of the American Chemical Society*, vol. 140, no. 8, pp. 2890–2896, 2018.

[36] K.-C. Hsiao, M.-H. Jao, K.-Y. Tian et al., "Acetamidinium cation to confer ion immobilization and structure stabilization of organometal halide perovskite toward long life and high-efficiency p-i-n planar solar cell via air-processable method," *Solar RRL*, vol. 4, no. 9, article 2000197, 2020.

[37] M.-C. Wu, T.-H. Lin, S.-H. Chan, Y.-H. Liao, and Y.-H. Chang, "Enhanced photovoltaic performance of perovskite solar cells by tuning alkaline earth metal-doped perovskite-structured absorber and metal-doped TiO2 hole blocking layer," *ACS Applied Energy Materials*, vol. 1, no. 9, pp. 4849–4859, 2018.

[38] M.-C. Wu, T.-H. Lin, S.-H. Chan, and W.-F. Su, "Improved efficiency of perovskite photovoltaics based on Ca-doped methylammonium lead halide," *Journal of the Taiwan Institute of Chemical Engineers*, vol. 80, pp. 695–700, 2017.

[39] C. F. J. Lau, X. Deng, J. Zheng et al., "Enhanced performance via partial lead replacement with calcium for a CsPbI3perovskite solar cell exceeding 13% power conversion efficiency," *Journal of Materials Chemistry A*, vol. 6, no. 14, pp. 5580–5586, 2018.

[40] C. F. J. Lau, M. Zhang, X. Deng et al., "Strontium-doped low-temperature-processed $CsPbI_2Br$ perovskite solar cells," *ACS Energy Letters*, vol. 2, no. 10, pp. 2319–2325, 2017.

[41] X. Shai, L. Zuo, P. Sun et al., "Efficient planar perovskite solar cells using halide Sr-substituted Pb perovskite," *Nano Energy*, vol. 36, pp. 213–222, 2017.

[42] R. Li, H. Zhang, X. Han, X. Huo, M. Zhang, and M. Guo, "Efficient nanorod array perovskite solar cells: a suitable structure for high strontium substitution in nature," *ACS Applied Materials & Interfaces*, vol. 12, no. 9, pp. 10515–10526, 2020.

[43] H. Zhang, W. Liu, R. Li, M. Zhang, and M. Guo, "Lead-less mesoscopic perovskite solar cells with enhanced photovoltaic performance by strontium chloride substitution," *Ceramics International*, vol. 44, no. 15, pp. 18863–18870, 2018.